Monthly Notices
of the
ROYAL ASTRONOMICAL SOCIETY

MNRAS **489,** 5709–5722 (2019)
Advance Access publication 2019 September 7

doi:10.1093/mnras/stz2494

Post-starburst galaxies in SDSS-IV MaNGA

Yan-Mei Chen,[1,2,3,4★] Yong Shi,[1,2,3] Vivienne Wild,[4] Christy Tremonti,[5] Kate Rowlands,[6] Dmitry Bizyaev,[7,8] Renbin Yan,[9] Lihwai Lin[10] and Rogério Riffel[11,12]

[1]*Department of Astronomy, Nanjing University, Nanjing 210093, China*
[2]*Key Laboratory of Modern Astronomy and Astrophysics (Nanjing University), Ministry of Education, Nanjing 210093, China*
[3]*Collaborative Innovation Center of Modern Astronomy and Space Exploration, Nanjing 210093, China*
[4]*School of Physics and Astronomy, University of St Andrews, St Andrews KY16 9SS, UK*
[5]*Department of Astronomy, University of Wisconsin-Madison, 1150 University Ave, Madison, WI 53706, USA*
[6]*Department of Physics and Astronomy, Johns Hopkins University, Bloomberg Centre, 3400 N. Charles St, Baltimore, MD 21218, USA*
[7]*Apache Point Observatory and New Mexico State University, PO Box 59, Sunspot, NM 88349-0059, USA*
[8]*Sternberg Astronomical Institute, Moscow State University, Moscow 119992, Russia*
[9]*Department of Physics and Astronomy, University of Kentucky, 505 Rose Street, Lexington, KY 40506-0055, USA*
[10]*Institute of Astronomy and Astrophysics, Academia Sinica, PO Box 23-141, Taipei 106, Taiwan*
[11]*Departamento de Astronomia, Instituto de Física, Universidade Federal do Rio Grande do Sul, Campus do Vale, 91501-970 Porto Alegre, Brasil*
[12]*Laboratório Interinstitucional de e-Astronomia, 77 Rua General José Cristino, 20921-400 Rio de Janeiro, Brasil*

Accepted 2019 September 2. Received 2019 August 15; in original form 2019 June 26

ABSTRACT

Post-starburst galaxies, identified by their unusually strong Balmer absorption lines and weaker than average emission lines, have traditionally been selected based on their central stellar populations. Here we identify 360 galaxies with post-starburst regions from the MaNGA integral field survey and classify these galaxies into three types: 31 galaxies with central post-starburst regions (CPSB), 37 galaxies with off-centre ring-like post-starburst regions (RPSB), and 292 galaxies with irregular post-starburst regions (IPSB). Focusing on the CPSB and RPSB samples, and comparing their radial gradients in D_n4000, $H\delta_A$, and $W(H\alpha)$ to control samples, we find that while the CPSBs have suppressed star formation throughout their bulge and disc, and there is clear evidence of rapid decline of star formation in the central regions, the RPSBs only show clear evidence of recently rapidly suppressed star formation in their outer regions and an ongoing central starburst. The radial profiles in mass-weighted age and stellar v/σ indicate that CPSBs and RPSBs are not simply different evolutionary stages of the same event, rather the CPSB galaxies are caused by a significant disruptive event, while the RPSB galaxies are caused by disruption of gas fuelling to the outer regions. Compared to the control samples, both CPSB and RPSB galaxies show a higher fraction of interactions/mergers, misaligned gas, or bars that might be the cause of the gas inflows and subsequent quenching.

Key words: galaxies: evolution – galaxies: star formation.

1 INTRODUCTION

The galaxy population in the local Universe is characterized by a clear bimodality in the colour–magnitude diagram (Baldry et al. 2004; Jin et al. 2014), with a 'blue cloud' (the gas-rich star-forming galaxies) and 'red sequence' (gas-poor quiescent galaxies). In between lies a minor population of 'green valley' galaxies. This bimodality has built up over cosmic time, with galaxies migrating from the blue cloud to the red sequence (Bell et al. 2004; Brown et al. 2007). The low galaxy number density in the green valley has been argued to imply that the migration is relatively rapid (Martin et al. 2007), however, the exact time-scales are still under debate (for a recent summary see Rowlands et al. 2018).

Post-starburst (PSBs) galaxies, also called E+A/K+A galaxies, show unusually prominent Balmer absorption lines indicating an excess contribution to their light from intermediate-age stars (A- or F-type stars). This can be due to a recent starburst or rapid decline in star formation (SF). Many such systems also show weak or absent nebular emission lines, implying an absence of the hotter, younger stars (O and B type). This implies an abrupt termination of the SF process (Dressler & Gunn 1983; Poggianti et al. 1999; Goto et al. 2003b). Many have postulated that PSBs are observed in a short-lived transition phase, providing an evolutionary link between the blue cloud and red-sequence galaxies (e.g. Yang et al. 2004, 2006;

★ E-mail: chenym@nju.edu.cn

Kaviraj et al. 2007; Wild et al. 2009; Yesuf et al. 2014; Cales & Brotherton 2015; Wild et al. 2016; Alatalo et al. 2016a; Rowlands et al. 2018), but whether this is true for most of PSBs remains unclear. In this paper we will use the term 'quenching' to refer to a recent rapid shut-off of SF and 'quenched' to refer to a galaxy or region of a galaxy with minimal current SF, regardless of whether this is a temporary or permanent state. A quenched galaxy by this definition, may subsequently form stars.

Since their discovery PSB galaxies have been extensively studied. Significant progress was made with the advent of high-quality multiobject spectroscopy, in particular with the SDSS (York et al. 2000) surveys, which identified PSB galaxies based on light from the central 3' diameter (Goto et al. 2003a; Goto 2005, 2007a; Yan et al. 2009). The morphology of PSB galaxies is found to be typically bulge dominated and sometimes with an underlying disc (Quintero et al. 2004; Tran et al. 2004; Goto 2005; Wong et al. 2012; Maltby et al. 2018; Pawlik et al. 2018). Disturbed morphologies or tidal features are present in many cases (e.g. Zabludoff et al. 1996; Goto 2005; Yamauchi, Yagi & Goto 2008; Yang et al. 2008; Lin et al. 2010; Sell et al. 2014; Pawlik et al. 2018), which fade rapidly with starburst age (Pawlik et al. 2016, 2019). The disturbed, bulge-dominated morphologies, as well as the elemental abundances (Goto 2007b), are consistent with the hypothesis that many of them are remnants of mergers or interactions, and the progenitors of early-type galaxies.

Much attention also has been given to PSB galaxies in dense environments, where the environment could give rise to their sudden change in SF activity. Studies of large galaxy clusters indicate an enhanced fraction of PSB galaxies compared to the field, at least in the cluster cores (Dressler et al. 1999; Poggianti et al. 1999; Tran et al. 2003, 2004; von der Linden et al. 2010; Socolovsky et al. 2018; Paccagnella et al. 2019), which implies environmental processes such as ram-pressure stripping or harassment may be at play. Mergers are not expected to be important in clusters due to the high relative velocities of the galaxies. However, it is important to realize that in the local Universe the vast majority of PSB galaxies are found in the field, with little trend with local density (Quintero et al. 2004; Balogh et al. 2005; Goto 2005; Hogg et al. 2006; Yan et al. 2009; Pawlik et al. 2018). This is again consistent with the majority of PSBs originating from mergers of star-forming galaxies, although additional processes may play a role in clusters.

While many PSB galaxies possess both morphological and spectroscopic signatures of an evolutionary transition, the significant reservoirs of cold gas found in recent studies (French et al. 2015; Rowlands et al. 2015; Alatalo et al. 2016b) have raised some doubt as to this simple interpretation. Additionally, the EAGLE cosmological hydrodynamic simulation reveals multiple evolutionary pathways for PSB galaxies in the local (simulated) Universe (Pawlik et al. 2019). Further studies are clearly needed to understand the origin and fate of these intriguing galaxies.

In particular, the stellar population gradients and internal kinematics are poorly understood. In the last few years small numbers of PSB galaxies have been studied with long slits or integral-field units (IFU) (Pracy, Couch & Kuntschner 2010; Swinbank et al. 2011; Pracy et al. 2013, 2014; Hiner & Canalizo 2015). Such studies are crucial to answer the most important question of active research: do the stellar population gradients and kinematics of PSB galaxies support the picture of galaxy mergers forming spheroids, or are they consistent with models in which SF is abruptly quenched in otherwise normal disc galaxies? The small samples, limited spectral, or spatial coverage, and poorer data quality of these studies compared to the SDSS surveys, have thus far precluded a comprehensive answer to this question.

Due to large sample of 4633 galaxies observed in the first three years of the fibre-optic IFU survey 'Mapping Nearby Galaxies at Apache Point Observatory' (MaNGA), for the first time, we are able to search for PSB regions within the complete galaxy area. We can identify off-centre PSB regions, ask what the difference is between these galaxies and galaxies with central PSB regions, and investigate the implications for their formation. In this paper we focus on galaxies with central and ring-like PSB regions. In Section 2, we introduce the MaNGA survey, sample selection, and data analysis methods. The properties of the galaxies with PSB regions, including the host galaxy morphology, stellar populations, and internal kinematics, are studied in Section 3. We discuss the observational results in Section 4 and a short summary is presented in Section 5. We use the cosmological parameters $H_0 = 70$ km s^{-1} Mpc^{-1}, $\Omega_M = 0.3$, and $\Omega_\Lambda = 0.7$ throughout this paper.

2 DATA

2.1 The MaNGA survey

MaNGA is one of the three major programs of the ongoing fourth-generation Sloan Digital Sky Survey (SDSS-IV; Bundy et al. 2015; Drory et al. 2015; Law et al. 2015, 2016; Yan et al. 2016a, b; Blanton et al. 2017), using 2.5m Sloan Foundation Telescope (Gunn et al. 2006) at Apache Point Telescope (APO). MaNGA employs dithered observations with 17 fiber-bundle IFUs with five sizes varying between 19 and 127 (or 12.5–32.5 arcsec diameter in the sky), depending on the apparent size of the target. Two dual-channel BOSS spectrographs (Smee et al. 2013) provide simultaneous spectral coverage over 3622–10 354 Å at $R \sim 2000$. Between 2014 and 2020, MaNGA will have obtained IFU observations of ∼10 000 galaxies ($z \leq 0.1$) with stellar mass $M_* \geq 10^9\,M_\odot$ and with an approximately flat M_* distribution (Wake et al. 2017). MaNGA will observe 2/3 of the galaxy sample out to $\sim 1.5R_e$ and the other 1/3 to $\sim 2.5R_e$. As described by Yan et al. (2016a), with a typical integration time of three hours, MaNGA reaches a signal-to-noise ratio (S/N) of four to eight per fiber in the *r*-band at a surface brightness of 23 ABmag arcsec^{-2}, which is the typical case for the outskirts of MaNGA targets. The 2 arcsec fiber diameter corresponds to a ∼1kpc spatial resolution at the peak redshift ($z \sim 0.03$) of the MaNGA sample.

2.2 Data analysis

The MaNGA sample and data products used here were drawn from the internal MaNGA Product Launch-6 (MPL-6), which includes ∼4633 galaxies observed through 2016 July (the first three years of the survey). The MaNGA data analysis pipeline (DAP, Westfall et al. 2019), which uses pPXF (Cappellari & Emsellem 2004) and a subset of stellar templates drawn from the MILES library (Sánchez-Blázquez et al. 2006), fits the stellar continuum in each spaxel and produces estimates of the stellar absorption lines, alongside measurements of 21 major nebular emission lines in the MaNGA wavelength coverage. In addition to analysing each individual spaxel, the DAP also builds spatially Voronoi-binned data cubes using the algorithm of Cappellari & Copin (2003), and performs the analysis on these binned spectra.

For this study we extract from the DAP products named 'SPX-GAU-MILESHC' (analysis of each individual pixel) the projected stellar rotation velocity (v_{star}), stellar velocity dispersion (σ_{star}), rotation velocity of ionized gas (v_{gas}), and velocity dispersion of ionized gas (σ_{gas}). From the Voronoi-binned data cubes named 'MAPS-VOR10-GAU-MILESHC', which are binned to S/N ∼

10 in *r*-band, we extract the spectral indices D_n4000 and $H\delta_A$, and nebular emission line fluxes and equivalent widths. Note that emission line fluxes and equivalent width values are corrected for underlying stellar continuum absorption. The index D_n4000 measures the strength of the 4000 Å break parametrized as the ratio of the flux density between two narrow continuum bands 3850–3950 and 4000–4100 Å (Bruzual 1983). The Lick Index $H\delta_A$ is the equivalent width of Hδ absorption feature in the bandpass 4083–4122 Å with continuum bandpasses of 4041.6–4079.75 and 4128.5–4161.0 Å (Worthey et al. 1994; Worthey & Ottaviani 1997).

The derived galaxy parameters required in this work include total stellar mass (M_*), light-weighted and mass-weighted stellar age, and Sérsic index. The total stellar mass was taken from the MPA-JHU catalogue.[1] The stellar *M*/*L* are obtained by comparing *u*, *g*, *r*, *i*, *z* colours of galaxies to a large grid of model galaxy colours following the methodology described in Brinchmann et al. (2004) and Tremonti et al. (2004). The light- and mass-weighted stellar ages are from MaNGA-Pipe3D value-added catalogue (Sánchez et al. 2016a, b). The Sérsic index are taken from MaNGA PyMorph photometric catalogue (Fischer, Domínguez Sánchez & Bernardi 2019).

2.3 Sample selection

There are multiple ways to select PSB galaxies. As described in Section 1, traditionally PSBs are identified based on the presence of strong Balmer absorption (an intermediate age stellar population) and weak or absent emission lines (e.g. Hα and/or [O II]) indicating no ongoing SF. Recent studies have challenged the strict limit placed on nebular emission lines, which biases the PSB selection against galaxies hosting narrow-line active galactic nuclei (AGNs) or shocks, and excludes galaxies that are post-starburst but not (yet) fully quenched (Yan et al. 2006; Wild et al. 2007, 2009; Kocevski et al. 2011; Alatalo et al. 2014; Yesuf et al. 2014). However, not selecting on emission lines means some PSBs are missed where their Balmer lines are indistinguishable from the star-forming population, and can lead to contamination from dust-obscured starbursts (Poggianti & Wu 2000; Wild et al. 2007).

In this work, we adjust the traditional method to identify galaxies with lower Hα nebular emission than expected for the strength of their Balmer absorption lines. This allows us to include galaxies in the process of shutting down their SF, which may still exclude spaxels containing gas excited by shocks or a central AGN. Fig. 1 shows the strong correlation between W(Hα) and $H\delta_A$ for a sample of galaxies from the SDSS Data Release 7 using central fibre spectroscopy. The SDSS-DR7 sample includes 192 678 galaxies from the MPA-JHU catalogue with *z* Warning = 0 and spectral median S/N > 10 per pixel, redshift in the range of $0.01 < z < 0.08$, and stellar mass in the range of $10^8 < M*/M_\odot < 10^{12}$. Overplotted are toy model evolutionary tracks created from Bruzual & Charlot (2003) spectral synthesis models assuming a Chabrier (Chabrier 2003) initial mass function (IMF), where the Hα emission is computed from the model spectrum Lyman continuum flux following appendix B in Hunter & Elmegreen (2004). The models have an exponentially declining SF rate with an e-folding time of $\tau \sim 5$ Gyr, then a second exponentially declining starburst is added after 6.5 Gyr of evolution. The tracks for bursts with a range of decline times are shown. We identify PSB spaxels where they lie below the starburst track with an e-folding time of 300 Myr

[1] https://wwwmpa.mpa-garching.mpg.de/SDSS/DR7/

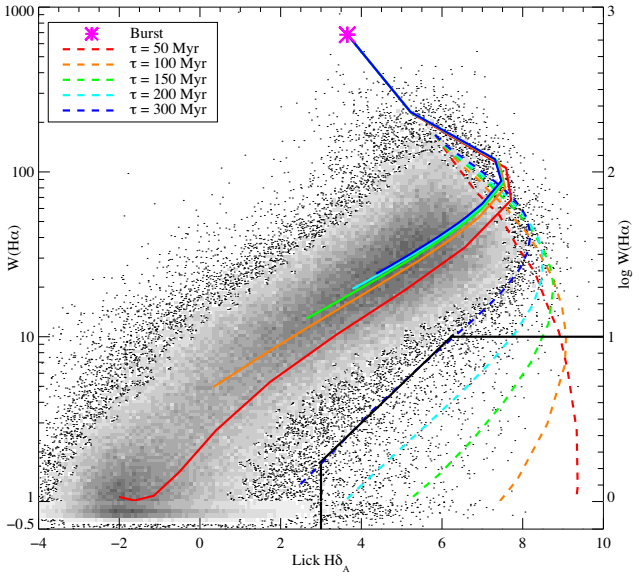

Figure 1. The $H\delta_A$ absorption line versus Hα emission line equivalent width for SDSS DR7 galaxies (greyscale) and toy model evolutionary tracks (coloured lines). The solid lines show exponentially declining SF histories with e-folding times of $\tau = 0.5$ Gyr (red) to $\tau = 5$ Gyr (blue). The dashed lines have an additional burst of SF after 6.5 Gyr, followed by truncation with e-folding times given in the legend. For all models the youngest point is marked by the magenta star, and they evolve to the bottom left over time. The black solid line indicates the region of our PSB selection box. *Y*-axis is in log-space when Hα emission line equivalent is larger than one and in linear space when it is smaller than one.

(marked by the black solid line), the same decline time found by Wild, Heckman & Charlot (2010) for central starbursts in the SDSS DR7. For this model, the W(Hα) falls to 10 Å after ∼1 Gyr.

In summary, we first require the spaxels to have a median spectral S/N > 10 per pixel, in order to obtain a robust measurement of $H\delta_A$. We then select a spaxel to be a PSB if it has $H\delta_A > 3$ Å, W(Hα)< 10 Å, and log W(Hα) $< 0.23 \times H\delta_A - 0.46$. Clearly the toy models should be taken as indicative only, with the previous SF history, burst mass fraction, and dust content of the galaxy playing a role in the true evolution of these spectral measurements. Our aim here is to select starburst regions that have recently and rapidly truncated their SF, but equally to include starburst regions that have not yet fully quenched their SF.

We identify 406/4633 galaxies with more than six contiguous spaxels that satisfy these selection criteria. Finally, a careful visual check was done to remove contaminants with foreground stars and background galaxies which affect the continuum fit. This reduces the sample to 360 galaxies. Fig. 2 shows four examples of galaxies with PSB regions. The left-hand panel shows the SDSS *g*, *r*, *i*-images; the middle panel shows the PSB regions in red; the spectrum located at the position of the white solid dot is shown in the right-hand panel, where the observed spectrum is in black and the best-fitting continuum models output by the MaNGA DAP is in red.

We visually classify these 360 galaxies into three types: galaxies with central post-starburst regions (CPSB, top row of Fig. 2), galaxies with ring-like post-starburst regions (RPSB, second and third rows of Fig. 2), and those with irregular outskirt PSB spaxels [irregular post-starburst regions (IPSBs), bottom row of Fig. 2]. The third galaxy is classified as RPSB since it is edge-on, and the two PSB regions in these RPSBs have similar rotation velocity with inverse rotation direction. In summary, we find 31 CPBs, 37 RPSBs,

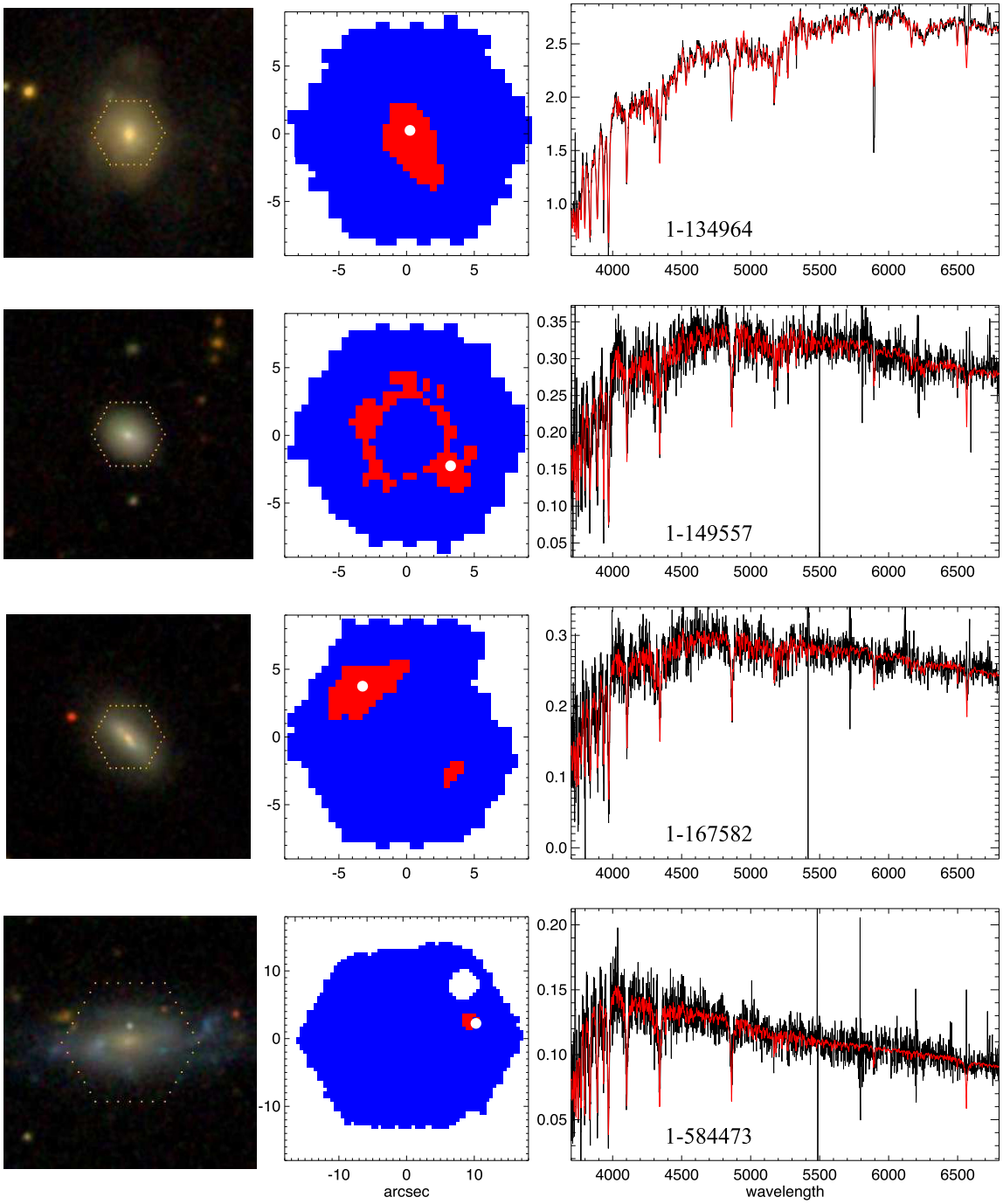

Figure 2. Examples of MaNGA galaxies with PSB regions, MaNGA ID for each galaxy is shown in the right-hand panel. The top row shows a galaxy with central post-starburst regions (CPSB). The second and third rows show galaxies with ring-like post-starburst regions (RPSB) and the bottom row shows a galaxy with an irregular region in the outskirts (IPSBs). For all four examples, the left-hand panel shows the SDSS *g*, *r*, *i*-image, the middle panel shows the post-starburst spaxels in red, the spectrum located at the position of the white solid dot is shown in the right-hand panel, with the observed spectrum in black and the best-fitting continuum model output by the MaNGA DAP in red.

and 292 IPSBs. We note that both the RPSBs and IPSBs are entirely new classes of PSBs.

The 31 CPSBs corresponds to a fraction of 0.7 per cent (31/4633) over the whole MaNGA sample. This low fraction is consistent with the results from Goto et al. (2003a) and Goto (2007b), who claim that the CPSB galaxies are a rare population (less than 1 per cent) in the local Universe, although the selection criteria is not exactly the same. The incidence of localized PSB regions is clearly a much more common phenomenon. These could be due to individual bright star clusters or cluster complexes with intermediate ages. We will leave the study of these objects to future work, and here focus on the CPSBs and RPSBs.

Table 1. The sample of CPSB galaxies. (1) MaNGA identifier; (2) Right ascension; (3) Declination; (4) log M_*; (5) D_n4000; (6) inclination for galaxies with low bulge fractions (fracDEV < 0.8); (7) Sérsic index; (8) slope of D_n4000 gradient; (9) slope of $H\delta_A$ gradient; (10) slope of logW($H\alpha$) gradient; (11) kinematic misalignment between gas and stars ($|PA_{kin,star} - PA_{kin,gas}|$); (12) notes of unusual features (EML = emission line).

MaNGAID (1)	RA (2)	Dec. (3)	logM_* (4)	D_n4000 (5)	i (6)	n (7)	∇_{D_n4000} (8)	$\nabla_{H\delta_A}$ (9)	$\nabla_{logW(H\alpha)}$ (10)	ΔPA_{kin} (11)	Features (12)
1–134964	246.76069	43.476100	10.95	1.54	–	3.2	0.100	− 2.963	0.286	25 ± 4	tidal tail
1–146344	120.06709	29.471437	9.97	1.49	–	2.0	0.099	− 1.900	0.143	180 ± 26	misaligned
1–149589	170.72345	51.341778	9.85	1.55	53	1.2	0.055	− 1.112	− 0.182	0 ± 20	–
1–149709	173.41287	52.674587	10.19	1.47	–	5.1	0.104	− 3.969	− 0.283	137 ± 7	misaligned
1–152474	114.45795	28.652892	8.85	1.53	3	1.6	− 0.054	− 0.437	0.244	–	no EML
1–163965	120.05960	26.698015	10.32	1.67	–	4.5	0.133	− 2.114	0.037	130 ± 7	misaligned
1–178374	260.61132	28.309696	10.78	1.60	–	8.0	0.055	− 0.991	− 0.222	–	tidal tail
1–178823	311.76380	0.43677787	9.40	1.60	53	–	0.473	− 3.173	− 0.447	150 ± 10	misaligned
1–179682	317.42261	0.62776940	9.45	1.57	–	7.2	0.079	− 2.818	− 0.191	–	no projected rotation
1–210114	242.58533	41.854895	10.74	1.57	–	8.0	0.042	− 1.604	− 0.529	–	tidal tail
1–248389	240.65805	41.293427	10.59	1.62	–	7.0	0.088	− 2.318	− 0.977	50 ± 4	tidal tail
1–250969	206.29627	42.319513	10.11	1.50	61	1.9	− 0.047	− 1.100	0.119	0 ± 11	bar
1–295343	246.48074	25.411607	9.91	1.57	–	5.0	0.099	− 2.730	0.658	180 ± 14	misaligned
1–29809	358.46882	− 0.0987309	9.45	1.59	43	1.5	0.029	− 1.901	− 0.317	143 ± 33	misaligned
1–301834	148.42110	35.701876	9.77	1.50	–	3.3	− 0.007	− 0.455	− 0.057	93 ± 16	misaligned
1–38062	49.228867	− 0.04200700	10.07	1.48	–	4.8	0.080	− 2.955	− 0.220	25 ± 9	disturbed gas velocity field
1–38166	49.946854	0.62382219	9.28	1.42	–	4.5	0.298	− 2.349	− 0.300	–	no projected rotation
1–38374	50.888599	− 0.43853564	9.88	1.59	69	1.5	− 0.012	− 1.018	0.228	93 ± 7	misaligned
1–384400	126.75586	21.706752	9.99	1.48	78	1.8	0.074	− 2.367	− 0.688	90 ± 4	misaligned
1–384486	127.31796	23.809021	9.28	1.52	–	6.5	0.153	− 6.250	0.699	–	no EML
1–385499	129.99929	23.413400	8.97	1.32	70	0.7	− 0.025	0.487	0.136	0 ± 11	–
1–404249	194.52342	29.017353	9.37	1.50	82	1.8	− 0.048	− 0.256	0.147	–	no EML
1–43584	117.06113	39.045731	8.91	1.26	81	0.7	− 0.099	1.137	0.545	12 ± 62	–
1–44447	120.63984	42.392705	10.04	1.56	–	3.5	0.096	− 2.585	− 0.365	18 ± 63	disturbed gas velocity field
1–456744	194.33162	27.613856	9.16	1.54	74	1.7	0.114	− 0.447	0.460	–	no EML
1–456850	194.63449	28.377961	8.62	1.42	44	1.3	0.204	2.281	0.885	–	no EML
1–457004	196.26374	27.537037	9.17	1.49	64	1.7	− 0.045	0.507	0.797	–	no EML
1–457130	195.33050	27.860463	9.02	1.35	3	2.0	0.174	− 1.345	− 0.842	–	no projected gas rotation
1–560826	236.16573	38.425357	11.03	1.61	32	5.2	0.192	− 3.816	− 0.448	–	tidal tail
1–72913	127.48937	44.940158	10.79	1.62	–	4.4	0.045	− 1.892	− 0.318	124 ± 37	misaligned
12–98126	230.50740	43.534632	9.69	1.59	43	5.7	− 0.075	2.678	0.140	–	no EML

2.4 Control samples

In order to quantify the difference between the PSB galaxies and typical galaxies, we built a control sample of galaxies without PSB regions. For each PSB, we select 10 control galaxies which are closely matched in stellar mass and global D_n4000. The global spectral indices are not produced as part of the DAP, therefore we stack the spectra across the full spatial extent of the MaNGA observations in order to measure them.

Our aim is to compare the PSB galaxies to plausible progenitors, therefore the motivation for choosing these two matching parameters is the following: (i) constraining the control galaxies to have similar stellar mass is extremely important because stellar population properties are known to vary strongly with stellar mass, (ii) constraining global D_n4000 ensures the control samples have stellar populations with similar light-weighted ages when averaged over the past few Gyr i.e. prior to any event that caused the post-starburst features. This match will not be perfect, as D_n4000 increases following a shutdown in SF, but avoids the need for extensive model-dependent spectral fitting that is beyond the scope of this paper.

3 RESULTS

Tables 1 and 2 list the samples of CPSB and RPSB galaxies, together with relevant parameters used in this paper. Figs 3 and 4 show examples of the spatially resolved stellar velocity, gas velocity, D_n4000, $H\delta_A$, and W($H\alpha$) maps of an example CPSB and RPSB galaxy that are broadly typical of the samples. The bottom panels show the radial gradients of the spectral indices, in units of the effective radius.

In the following sections we discuss the global properties of the CPSB and RPSB host galaxies, their kinematics and stellar populations. We are interested in understanding whether the new RPSB population is related to the CPSB population, and whether the spatially resolved maps are consistent with the hypothesis that CPSB galaxies are caused by major mergers.

3.1 Global population properties

The left-hand panel of Fig. 5 shows the CPSBs and RPSBs on the global D_n4000–stellar mass relation as the red and blue dots, respectively. The contours show the SDSS DR7 sample (as

Table 2. The sample of RPSB galaxies. (1) MaNGA identifier; (2) Right ascension; (3) Declination; (4) log M_*; (5) D_n4000; (6) inclination for galaxies with low bulge fractions (fracDEV < 0.8); (7) Sérsic index; (8) slope of D_n4000 gradient; (9) slope of $H\delta_A$ gradient; (10) slope of $\log W(H\alpha)$ gradient; (11) kinematic misalignment between gas and stars ($|PA_{kin,star} - PA_{kin,gas}|$); (12) notes of unusual features (EML = emission line).

MaNGAID (1)	RA (2)	Dec. (3)	logM_* (4)	D_n4000 (5)	i (6)	n (7)	∇_{D_n4000} (8)	$\nabla_{H\delta_A}$ (9)	$\nabla_{\log W(H\alpha)}$ (10)	ΔPA_{kin} (11)	Features (12)
1–134004	238.44858	47.404958	9.38	1.48	57	1.4	0.136	− 0.978	− 0.548	149 ± 22	misaligned
1–149557	171.77902	51.131645	9.15	1.42	38	1.4	0.102	− 1.137	− 0.703	156 ± 87	misalign
1–153247	119.36531	33.257935	8.94	1.44	59	1.7	0.088	− 2.071	− 0.703	149 ± 90	misaligned
1–167582	154.48083	46.603286	9.94	1.37	69	1.5	0.122	− 1.391	− 0.994	43 ± 18	misaligned
1–201355	117.05387	28.225092	10.14	1.30	3	–	0.073	0.789	− 0.441	6 ± 8	interacting/ pre-merger
1–211002	247.14945	39.719740	9.70	1.49	37	0.7	0.090	0.044	− 0.544	32 ± 16	misaligned
1–216976	135.75897	40.433985	10.60	1.45	6	4.5	0.257	− 3.853	− 1.487	–	tidal tail
1–217015	136.11419	41.486207	9.18	1.36	51	1.8	0.053	− 0.065	− 0.249	6 ± 17	tidal tail
1–217221	138.75315	42.024390	10.27	1.23	64	1.0	0.104	0.874	− 0.572	0 ± 4	disturbed gas velocity field
1–258306	183.57898	43.535279	9.54	1.24	72	2.1	0.150	0.552	− 0.960	12 ± 11	disturbed gas velocity field
1–258380	181.54597	45.149206	10.96	1.43	–	4.0	0.031	− 0.464	− 0.477	0 ± 4	–
1–277246	166.18780	45.156430	9.37	1.52	20	1.6	0.246	− 2.150	− 0.937	–	face-on, no projected rotation
1–277691	164.58519	40.788234	9.63	1.34	76	0.7	0.002	− 0.005	− 0.031	0 ± 9	edge-on
1–29512	356.75183	− 0.4473874	11.13	1.34	–	4.2	0.163	1.470	− 0.471	0 ± 7	bar
1–321354	218.94756	47.007467	9.59	1.31	66	1.6	0.134	− 1.272	− 0.264	6 ± 15	edge-on
1–373878	228.41485	28.244461	9.94	1.28	87	1.1	0.083	0.403	− 0.814	0 ± 13	interacting/ pre-merger
1–37862	47.029452	0.4562083	10.96	1.41	–	6.0	0.066	− 0.250	− 0.399	12 ± 4	tidal tail
1–38041	49.457454	− 0.5546585	9.94	1.52	66	1.4	0.187	− 3.188	− 1.609	124 ± 10	misaligned
1–38168	49.929339	0.5654778	10.06	1.28	–	5.6	0.182	0.765	− 1.115	0 ± 11	interacting/ pre-merger
1–38470	51.708914	0.19858883	9.74	1.34	–	5.3	0.115	− 0.722	− 0.032	12 ± 18	tidal tail
1–386695	137.98351	27.899270	10.11	1.31	76	1.3	0.152	1.440	− 0.686	7 ± 11	bar
1–387081	139.17787	28.054233	10.27	1.41	86	1.0	0.095	− 0.594	− 0.877	18 ± 16	edge-on
1–392007	154.97835	36.325739	10.20	1.49	72	2.4	− 0.021	− 0.003	− 0.202	6 ± 4	edge-on
1–405760	196.10272	36.479950	10.30	1.48	87	1.0	− 0.048	− 0.394	− 0.751	178 ± 4	misaligned
1–419380	183.00790	35.404399	9.89	1.41	57	3.6	0.290	− 3.467	− 1.290	172 ± 6	misaligned
1–456309	194.76938	26.958192	9.42	1.47	73	4.1	0.013	2.594	0.262	–	no EML
1–456915	194.73314	27.833445	10.54	1.51	87	0.8	− 0.164	1.821	− 0.043	18 ± 4	disturbed gas velocity field
1–457200	196.47287	28.112434	10.29	1.43	71	1.7	0.036	− 0.200	− 1.348	18 ± 12	bar
1–548626	120.55787	37.150076	10.66	1.40	87	1.4	− 0.152	2.877	− 0.627	0 ± 4	interacting/ pre-merger
1–558926	140.41142	43.726152	10.38	1.41	66	1.2	0.057	− 0.942	− 0.409	0 ± 4	tidal tail
1–574504	123.82033	46.075253	10.50	1.26	62	–	0.415	4.120	− 1.183	12 ± 4	bar
1–585632	143.51035	50.027486	10.45	1.54	23	2.4	− 0.007	0.835	− 0.946	–	interacting/ pre-merger
1–606105	147.66431	44.331163	9.48	1.47	60	1.9	0.114	− 2.462	− 1.336	31 ± 40	misaligned
1–625070	198.78425	30.403775	10.35	1.37	43	1.0	0.149	1.232	− 0.984	12 ± 4	bar
1–626502	203.05706	26.949981	10.52	1.48	74	1.2	0.058	0.163	− 1.133	0 ± 4	bar
1–630590	218.97634	53.391637	10.36	1.53	75	1.0	0.075	− 0.129	− 1.061	0 ± 6	bar
1–633000	233.23196	42.438257	10.10	1.46	64	2.0	0.118	− 1.098	− 0.999	156 ± 18	misaligned

described in Section 2.3), while the grey dots show the full MaNGA sample. For the MaNGA galaxies, D_n4000 is measured from the global spectrum, whereas for the SDSS DR7 sample, D_n4000 is measured from the central fibre spectroscopy. We choose to show D_n4000 rather than SFR or sSFR as it can be measured consistently for all galaxies. Plotting global SFR from the MPA-JHU catalogue instead of D_n4000 provides qualitatively the same picture, but relies on extrapolation of the fibre measurements using galaxy colours which we found to be biased for the PSB galaxies in MaNGA. It is clear that most RPSBs are located on the star-forming main sequence while the CPSBs are primarily located in the green valley, between the red and blue sequence.

Fischer et al. (2019) fit all the MaNGA DR15 galaxies with a single Sérsic profile, released as part of the MaNGA PyMorph catalogue. The right-hand panel of Fig. 5 shows the distribution of Sérsic index (n) for CPSBs (red) and RPSBs (blue). These values are reproduced in Tables 1 and 2 for the CPSB and RPSB samples, respectively. A higher fraction of the CPSB galaxies than RPSB galaxies have $n > 3$, consistent with disc-free elliptical galaxies. However, both samples cover a wide range of values indicating both types are hosted by galaxies with diverse morphologies. This is consistent with results found for CPSBs in SDSS DR7 (Pawlik et al. 2018).

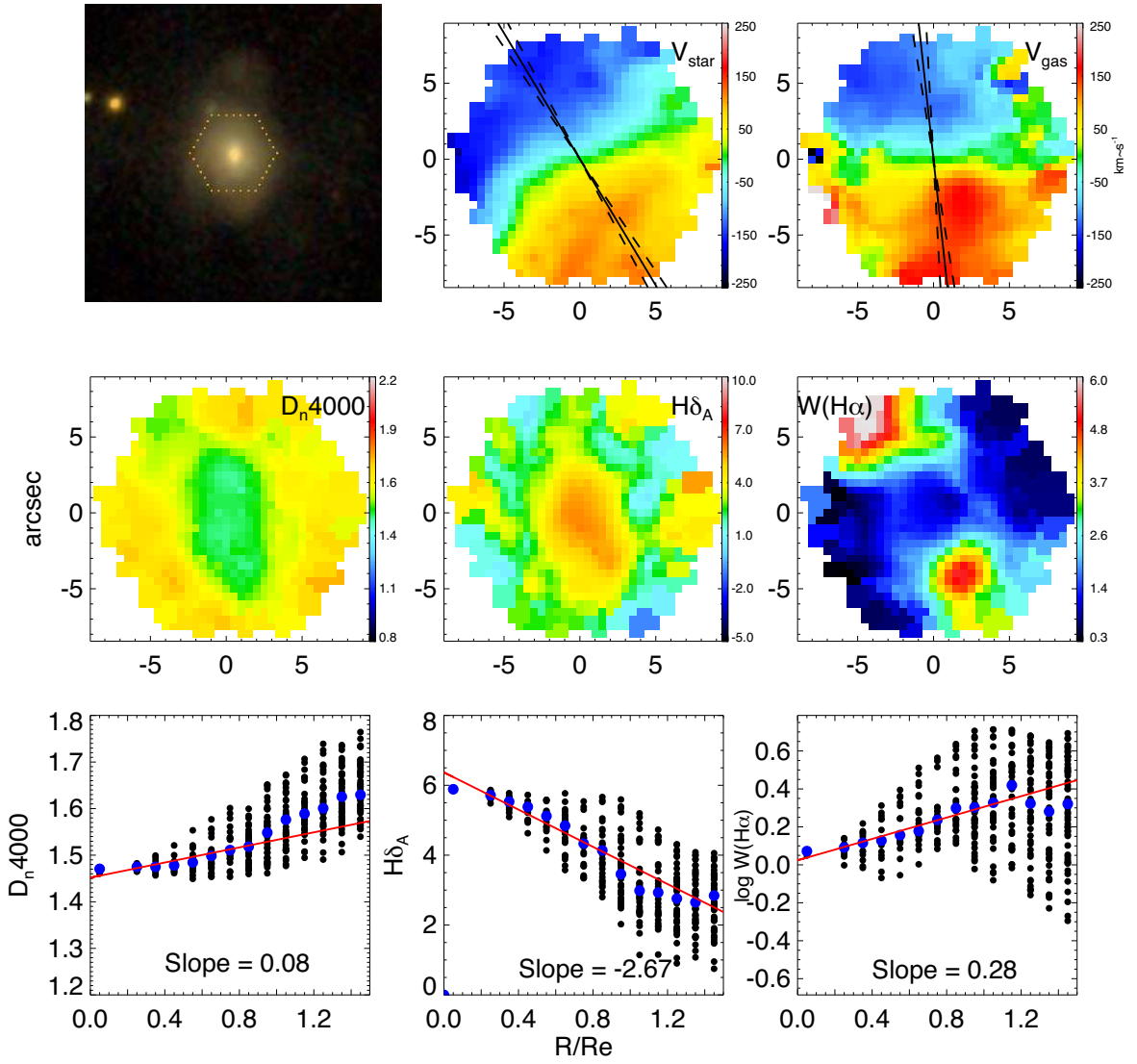

Figure 3. The spatially resolved stellar velocity, gas velocity, D_n4000, $H\delta_A$, and W(H α) of an example CPSB galaxy, MaNGA ID: 1–134964. *Top:* the SDSS three-colour image, stellar and gas velocity fields. The solid line overplotted on each velocity field shows the kinematic position angle, with the two dashed lines showing the 1σ error range. *Middle:* the D_n4000, $H\delta_A$, and W(H α)maps. *Bottom:* the radial profiles of D_n4000, $H\delta_A$, and W(H α). The black dots show the parameter value of each spaxel, and the blue dots show the median values in bins of 0.1 R_e. The red solid line is a linear fit to the binned median values, with the value of the fitted slope given in each panel.

3.2 Stellar populations

In this section, we study the stellar population distribution of the galaxies with PSB regions using continuum spectral indices D_n4000 and $H\delta_A$ as well as the H α emission line. Figs 3 and 4 show maps and radial profiles of D_n4000, $H\delta_A$, and W(H α) for the example CPSB and RPSB galaxies. These galaxies are typical of their classes, and the maps immediately illustrate the primary differences between them.

The top panel of Fig. 6 shows the averaged radial profiles of D_n4000, $H\delta_A$, and W(H α) for the CPSB (red solid line) and RPSB (blue solid line) samples. The error bars show the 30 per cent to 70 per cent percentile of the distributions for the CPSBs and RPSBs. The relevant control samples are shown as dashed lines. The bottom panel shows the distributions of the radial profile gradients of D_n4000, $H\delta_A$, and logW(H α). These slopes are reproduced in Tables 1 and 2. Both the CPSB and RPSB samples have positive gradients in D_n4000, indicating younger stellar populations in the central regions, with CPSBs having older stellar populations (higher D_n4000) on average than RPSBs across the entire galaxy. However, the CPSB and RPSB samples differ in their radial profiles of both $H\delta_A$ and W(H α): while in the CPSBs the Balmer absorption decreases with radius and W(H α) is weak or absent and almost flat, the RPSBs show strong Balmer absorption over the whole galaxy, while the W(H α) is strong in the centre and decreases sharply with radius. We have verified that the central H α emission in the RPSBs is primarily contributed by ongoing SF rather than shocks or AGNs: 33 of 37 RPSBs show star-forming/composite-like line ratios on the most commonly used Baldwin, Phillips & Terlevich (1981) diagram of [N II]/H α versus [O III]/H β flux ratios (Kewley et al. 2001; Kauffmann et al. 2003).

It is the differing radial gradients that lead to the different classifications of central or ring-like PSB: the CPSBs are typically only classified as PSBs in the centre, as their Balmer absorption

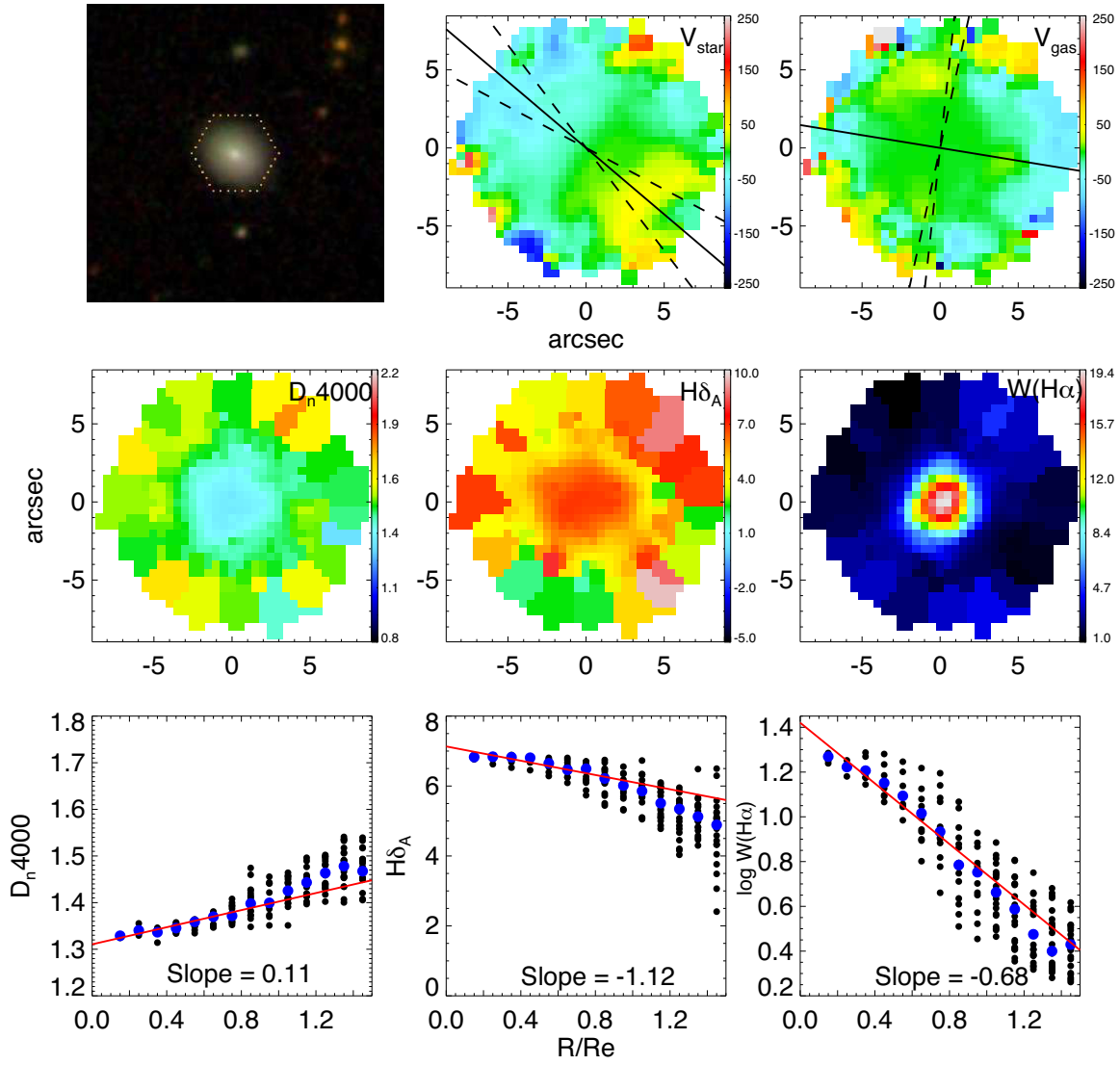

Figure 4. The same as Fig. 3 for an example RPSB galaxy, MaNGA ID: 1–149557.

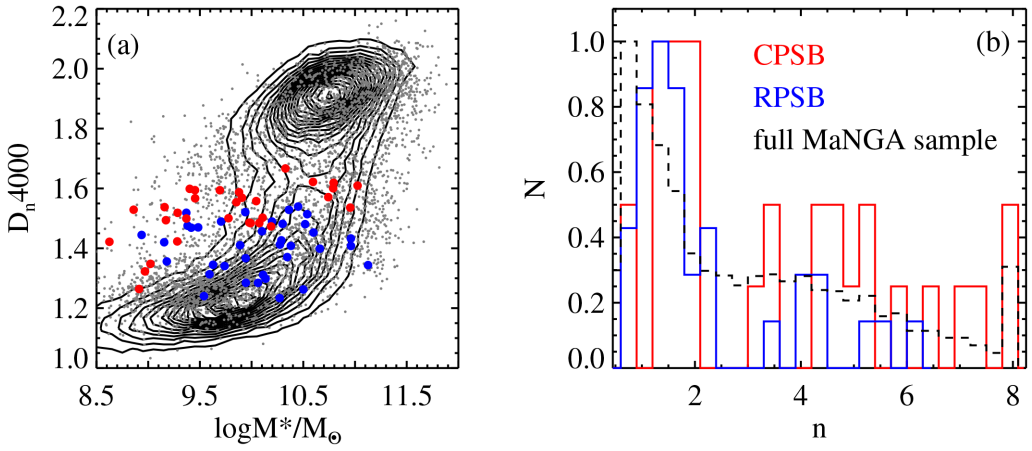

Figure 5. *Left:* The global D_n4000–stellar mass relation for the CPSB and RPSB galaxies (red and blue dots, respectively), with the SDSS DR7 sample as contours and full MaNGA sample as grey dots. *Right:* The Sérsic index distribution for the RPSB and CPSB galaxies are shown as blue and red histograms, respectively. The black dashed line shows the full MaNGA sample.

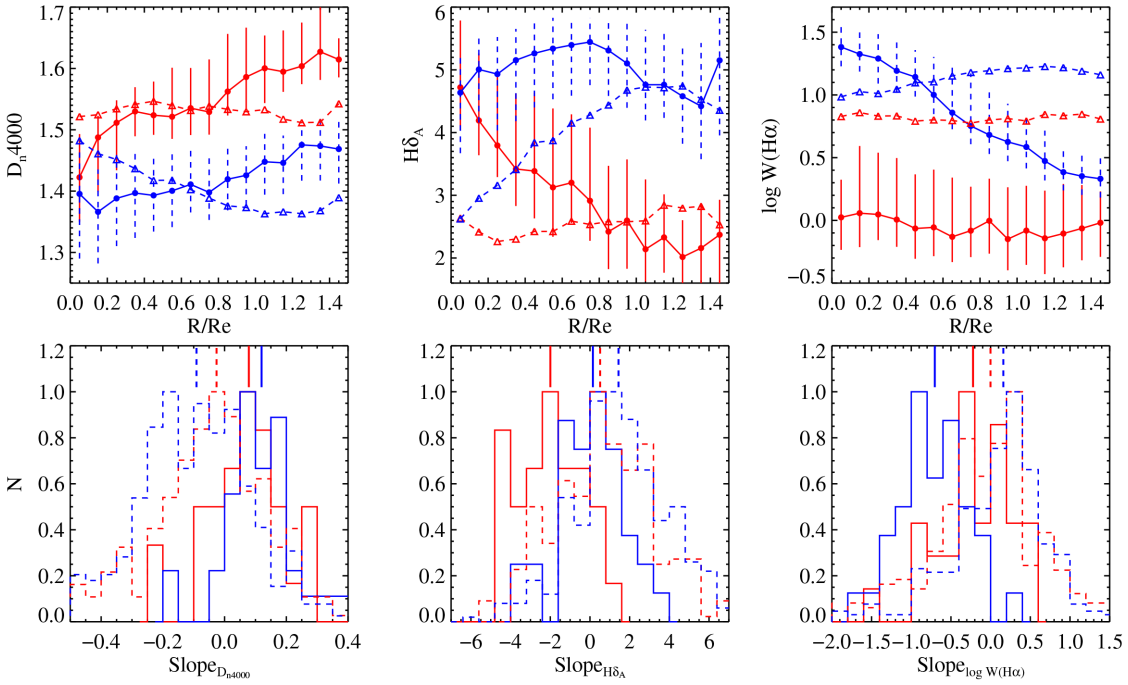

Figure 6. *Top panel:* Radial gradients of D$_n$4000, Hδ_A, and W(Hα) for the CPSB (red solid line), RPSB (blue solid line) as well as their control samples (red dashed and blue dashed lines). The error bars show the 30 per cent to 70 per cent percentile of the distributions for the CPSBs and RPSBs. *Bottom panel:* The distributions of the slope of D$_n$4000, Hδ_A, and W(Hα) for the four samples; the median values are shown as vertical lines on the top of each panel.

weakens with radius, whereas the RPSBs are not classified as PSBs in the centre due to their strong central W(Hα). This shows that while the CPSBs have suppressed SF throughout their bulge and disc, and clear evidence of rapid quenching (i.e. strong Balmer absorption) only in the central regions, the RPSBs only show clear evidence of recently rapidly suppressed SF in their outer regions. This difference in central SF also explains the different locations of the two populations in the global D$_n$4000–stellar mass relation with the RPSBs being located in the star-forming main sequence.

The stellar population gradients for the control samples are also shown in Fig. 6 as dashed lines and triangles. For the CPSBs, we find that their D$_n$4000 profiles are slightly more positive on average than the control sample, consistent with a recent centrally concentrated SF episode occurring in the past several Gyr. However, the weak W(Hα) compared to the controls indicates that ongoing SF has been strongly suppressed across the whole disc. The excess of Balmer absorption in the central regions of the CPSBs further indicates that a rapid shutdown in SF has occurred in the last Gyr, which is not seen in the controls. The RPSBs differ from their controls in all three indices, with the controls having a negative gradient in D$_n$4000 and a strong positive gradient in Hδ_A, indicating older stellar populations in the centre, as expected for ordinary bulge-dominated star-forming galaxies. The controls also show a constant W(Hα) with radius, indicating ongoing SF throughout the galaxy, significantly different from the sharp decline with radius seen in the RPSBs. We can see that Hδ_A $\sim$ 5 Å is not unusual in the outer regions of ordinary star-forming galaxies; it is only the combination of strong Balmer absorption and weak emission line strength that makes the outer regions of the RPSBs stand out. The Hδ_A $\sim$ 5 Å in the central region of the RPSBs is consistent with ongoing SF rather than a quenched population (see Fig. 2). Compared to the control samples, this ongoing SF is significantly stronger, perhaps indicating a time-limited starburst rather than more ordinary long-term SF.

There are several possible scenarios that could cause the observed radial gradients in stellar populations of the two samples. It is possible that either the outer regions of the CPSBs never underwent a starburst, or that the post-starburst is fading more quickly with increasing radius, which in turn could imply either that the burst was weaker in the outer regions, or that it occurred earlier. For the RPSBs, the starburst nature of the central regions combined with the quenching of the outer regions suggests that either a starburst has migrated from the outside inwards, or that the process that caused a central starburst has similarly led to the depletion of gas in the outer regions, potentially through strong gas flows from the outside-in.

Fig. 7 shows the radial gradients in light-weighted and mass-weighted stellar age for the PSB samples and their controls, from the Pipe3D Value Added Catalog (Sánchez et al. 2016a, b). Since D$_n$4000 is a good indicator of light-weighted age of a stellar population, the radial gradients of light-weighted age and D$_n$4000 are similar. Light-weighted age enhances the differences between the central regions of the PSBs and the control samples, due to the large fraction of very young stars which dominate the light-weighted age more than they contribute to D$_n$4000. Interestingly, the mass-weighted ages of the RPSB galaxies indicate a substantial old stellar population in their centres (8 Gyr), consistent with the control sample. This suggests the current central SF is simply a 'frosting' on top of a dominant old central population. The mass-weighted age profiles of the CPSBs indicate a very different history, with a higher fraction of stellar mass formed more recently throughout the whole galaxy compared to both control samples and the RPSBs. The very different behaviors in the mass-weighted age of CPSBs and RPSBs indicate that they have very different SF histories, thus it is impossible for the RPSBs to evolve into CPSBs through secular process. Equally, the similarity in mass-weighted age between the two control samples, contrasted with the difference in the CPSBs, supports significant disruption of the stellar component during the

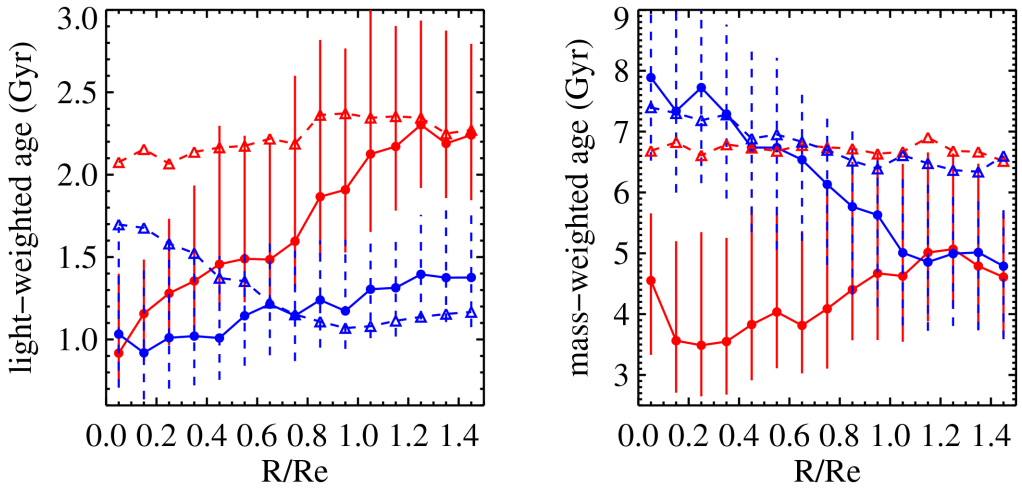

Figure 7. Average light-weighted and mass-weighted stellar age of the PSB samples and their controls. The symbols and lines are the same as that in Fig. 6.

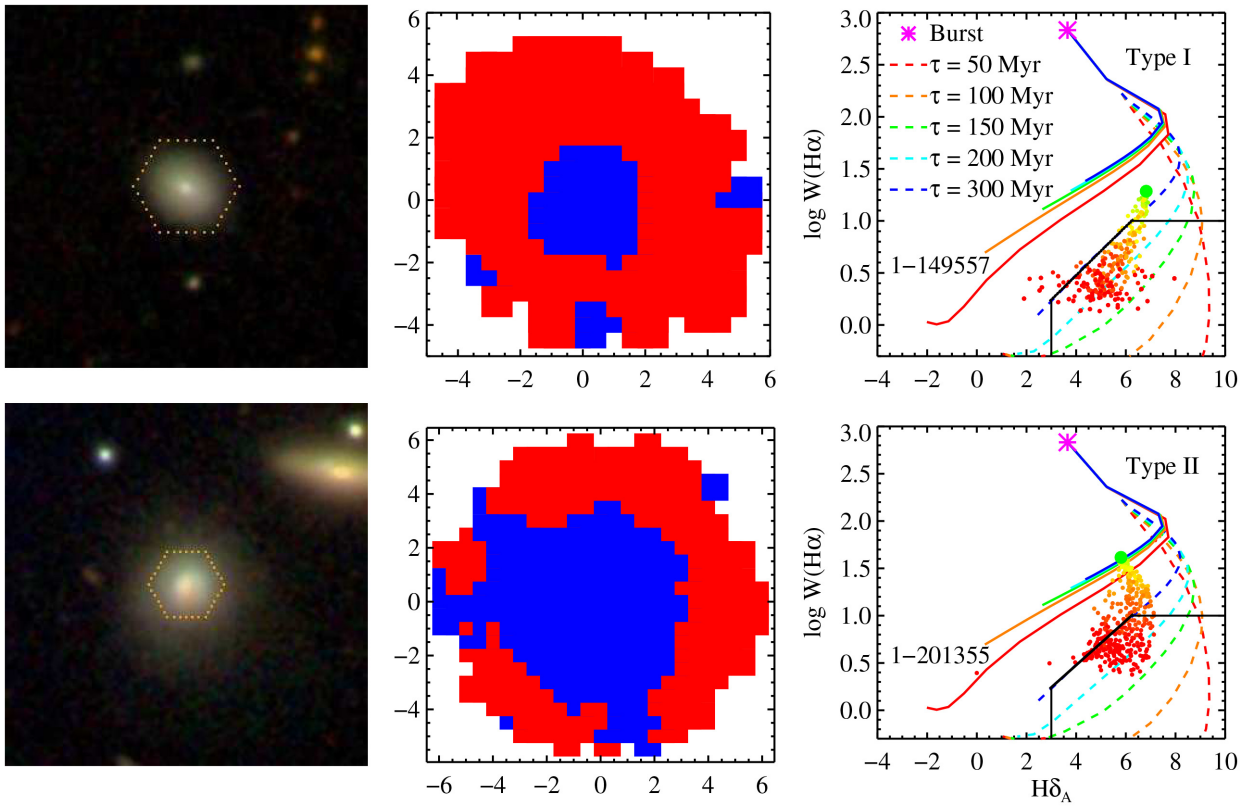

Figure 8. Examples of RPSBs on the Hδ_A versus W(Hα) plane; MaNGA ID of each galaxy is shown in the right-hand panel. We separate RPSBs into type I (top) & II (bottom). From left to right we show: the SDSS false-colour images; the PSB regions in blue; the galaxy spaxels in the Hδ_A versus W(Hα) plane. The solid and dashed lines are model evolutionary tracks (see Fig. 1). The data points are colour-coded by R/R_e with the larger green point marking the central pixel and the radius increases as the points become redder. The black lines mark the PSB selection criteria.

event that triggered the post-starburst features. Such a disruption event is not as evident in the RPSB sample.

Finally, we investigate the distribution of PSB spaxels in the Hδ_A versus W(Hα) plane for the RPSB galaxies with data points colour-coded by R/R_e. Fig. 8 shows examples of two seemingly different classes of RPSB galaxies. At the top (type I) the entire galaxy lies below the star-forming main sequence, with spaxels falling diagonally along the constant-burst-strength model track. At the bottom (type II), the spaxels fall vertically, with the central region still lying on the star-forming main sequence, while the outer spaxels have lower W(Hα).

The type I RPSBs appear to be undergoing a global shutdown in SF, similar to that seen in the CPSBs but less complete, and is consistent with our constant-burst-strength models with the starburst occurring first in the outer regions of the galaxy and moving inwards over time. Alternatively, the outer regions could

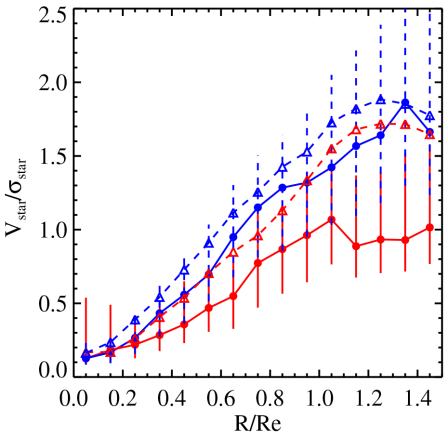

Figure 9. Averaged V_{star}/σ_{star} versus the radius for CPSB (red solid line) and RPSB (blue solid line) samples, as well as their control samples (red dashed and blue dashed lines). The error bars indicate the 30th and 70th percentiles of the distribution.

be quenched first, for example due to strangulation processes where the infall of fresh gas is shut off.

The type II RPSBs are consistent with having a range of quenching time-scales, with the outer regions quenching more quickly than the inner regions. It is possible that the inner regions will continue to form stars following the event that caused the outer regions to quench. Alternatively these galaxies are undergoing a rapid quenching following a starburst that occurred earlier in the outer regions than the inner regions, similar to the Tpye I RPSBs, but at a later time than the 6.5 Gyr assumed by our toy models (moving the red dashed line to the left). This type could be caused by ram pressure stripping – the outer regions are most vulnerable to being stripped and quench the quickest. Or they might be linked to mergers or interactions that cause the gas in the galaxies' outskirts to flow inwards causing a central starburst and rapid outer quenching.

Again, the question is whether these two types are evolutionarily linked, with type II being younger than type I, or whether they are caused by distinct processes. With more extensive modelling, the current PSB samples may provide a way to disentangle various suggested quenching mechanisms.

3.3 Kinematics and morphological features

In the present-day Universe, the majority of galaxies (>85 per cent) are consistent with being axisymmetric rotating oblate spheroids and only a minor fraction of galaxies have complex dynamics (for a review, see Cappellari 2016). The ratio of ordered to random stellar motion in galaxies has a strong dependence on luminosity or stellar mass (Illingworth 1977; Davies et al. 1983; Emsellem et al. 2011; Brough et al. 2017; van de Sande et al. 2017; Veale et al. 2017; Green et al. 2018), which suggests a link between the build-up of stellar mass and angular momentum over time. Major mergers are key candidates leading to a dramatic change in the morphology and spin of galaxies, but ultimately mergers are only one of many physical processes at play, and continuing gas accretion and SF can reshape the remnant morphology and kinematics (Naab et al. 2014, and citations therein).

Fig. 9 shows the average stellar velocity to dispersion ratio, v_{star}/σ_{star}, versus radius for the CPSB (red solid) and RPSB (blue solid) galaxies, as well as their control samples (red and blue dashed lines). The error bars indicate the 30th and 70th percentiles of the distribution. v_{star} and σ_{star} are calculated from the spectral fitting described in Section 2.2. A higher (lower) value of v_{star}/σ_{star} corresponds to more (less) rotational support, and therefore this plot can help us to discern any difference in the formation/interaction history of the PSB samples. Comparing Fig. 9 with fig. 2 of Emsellem et al. (2007), we find that the averaged v/σ radial profiles are consistent with fast rotators for all four samples, which is not surprising given the high mass and rareness of slow rotators. However, the CPSBs have noticeably lower v/σ than the other three samples, while the RPSB galaxies are much more consistent with their control sample. This indicates that the CPSBs have suffered from more frequent and/or violent interactions, mergers, or gas accretion processes (Lagos 2018).

Such processes can also lead to the inflows of gas required to induce both the excess central SF in the RPSB galaxies compared to their controls, and the central post-starbursts in the CPSB galaxies. For example, accretion of counterrotating gas from a gas-rich dwarf or the cosmic web on to a star-forming galaxy will lead to the re-distribution of angular momentum from gas–gas collisions between the pre-existing and the accreted gas, which greatly accelerates gas inflow (Chen et al. 2016). However, additional processes such as bars may play a role (Hawarden et al. 1986; Lin et al. 2017; Chown et al. 2019).

In order to understand the possible prevalence of such mechanisms in the PSB samples, we investigate the kinematic misalignment between stars and ionized gas, measured as the difference in the kinematic position angle, $\Delta PA_{kin} = |PA_* - PA_{gas}|$, where PA_* is the kinematic position angle of the stars and PA_{gas} is the kinematic position angle of the ionized gas. The kinematic PA is measured using FIT_KINEMATIC_PA[2] (Krajnović et al. 2006), and is defined as the counterclockwise angle between north and a line that bisects the velocity field of gas or stars, measured on the receding side. The solid lines in the top row of Figs 3 and 4 show the best-fitting position angle to our example galaxies, while the two dashed lines show the $\pm 1\sigma$ error. The example CPSB galaxy is a star–gas misaligned galaxy with $\Delta PA_{kin} = 25$ deg, while the example RPSB shows no regular rotation in ionized gas. The values are listed in Tables 1 and 2 for the CPSBs and RPSBs, respectively. There are 13 CPSBs and four RPSBs without ΔPA_{kin} measurements either due to no emission lines or no obvious rotation; we do not consider them in the analysis of misaligned kinematics.

Additionally we use deep images to identify bars, tidal tails, and other interaction features in our samples. We use the Legacy Surveys,[3] which combines imaging projects on different telescopes, including the Beijing–Arizona Sky Survey (BASS), the DECam Legacy Survey (DECaLS), and the Mayall z-band Legacy Survey (MzLS). The images are one to two magnitudes deeper than SDSS. Our visual classifications are given in the final column of Tables 1 and 2.

The top panel of Fig. 10 shows the distribution of ΔPA_{kin} for CPSB (red) and RPSB (blue) samples, while the ΔPA_{kin} distribution of the control samples are shown in the bottom panel. Of the 17 CPSB galaxies for which we have both stellar and emission line kinematic measurements, 10 are misaligned (defined as $\Delta PA_{kin} \geq 30$ deg). A further seven show other signs of disturbance such as tidal tails or disturbed gas velocity fields. For the 33 RPSBs with both stellar and emission line kinematic measurements, 10 of them have misaligned gas and stellar kinematics, and a further

[2] https://www-astro.physics.ox.ac.uk/ mxc/software/
[3] http://legacysurvey.org

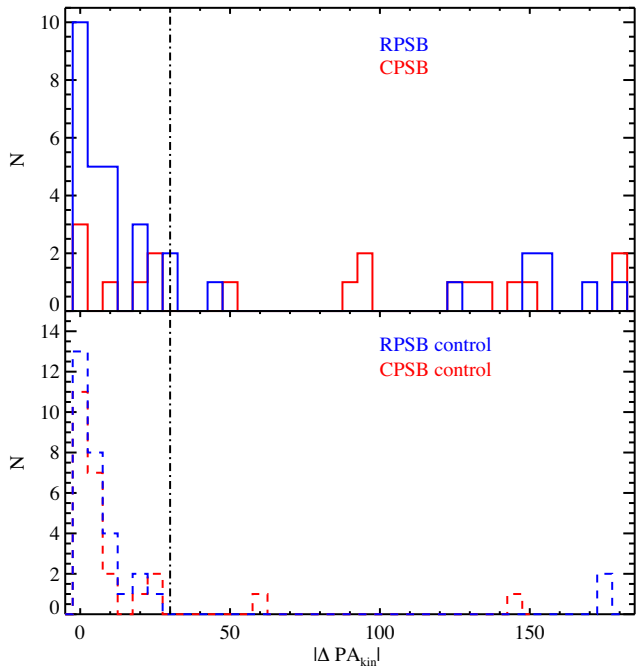

Figure 10. The distribution of ΔPA_{kin} ($=|PA_* - PA_{gas}|$) for CPSB (red) and RPSB (blue) samples in the top panel and the relevant control samples in the bottom panel. The vertical black lines mark the place where $\Delta PA_{kin} = 30$ deg, typically used to delineate 'normal' from 'misaligned' rotation.

13 show other interaction features. Therefore, we conclude that $\gtrsim$50 per cent of both CPSB and RPSB galaxies have evidence for kinematic or morphological disturbance. For the CPSB control samples, on average we find 1/31 galaxies with interaction evidence, and 3/31 galaxies with misaligned gas and stellar kinematics. For the RPSB control samples, on average we find 1/37 misaligned galaxy and no interaction evidence. The obvious difference between PSB galaxies and their control samples suggests that mergers, interaction, or recent gas accretion may plausibly cause the formation of PSB regions.

4 DISCUSSION

The optical spectral features of PSB galaxies have been interpreted as a signature of an abrupt decrease in the SF activity, likely following a recent starburst. This means that PSB regions have rapidly quenched their SF in the recent past and we can extrapolate to hypothesize that they are in transition from the blue cloud to the red sequence. Thus, they provide a unique insight into galaxy evolution and may offer a means of constraining the origin of the bimodal colour distribution of galaxies. However, the most direct and important problems regarding PSBs include: (1) what triggers the starburst at the beginning? (2) what mechanism quenches the starburst on the short time-scales (of order a single dynamical period) required to produce the PSB features?

To address these two questions, much work has been done in the past decade. Based on hydrodynamic simulations, a popular galaxy evolutionary picture has emerged in which two gas-rich discs merge, tidal torques channel gas to the galaxy centres and progress to heavily dust-obscured central starbursts, which is coupled with supermassive black hole (SMBH) fuelling and subsequent expulsion of gas, leading to the development of quiescent spheroids (e.g. Hopkins et al. 2006). The PSB phase can be fit into this picture as feedback clears out the leftover gas, both SF and black hole growth are ceased, and the galaxies pass through the post-starburst phase before they become 'red and dead'.

Observational evidence supporting this picture includes the high level of morphological disturbance in local PSB galaxies (Section 3.3 and Zabludoff et al. 1996; Yang et al. 2004, 2008; Pawlik et al. 2018), and fast outflowing gas detected in the Mg II 2796, 2803 absorption lines of $z > 0.5$ PSBs (Tremonti, Moustakas & Diamond-Stanic 2007), which may be a fossil galactic wind launched at the quasi-stellar object stage. However, the low stellar mass of local PSBs, as well as the absence of powerful AGNs in the local Universe makes this scenario less plausible for our sample. Additionally, the presence of cold gas in many PSBs shows that the gas has not been effectively expelled (French et al. 2015; Rowlands et al. 2015). The limited resolution of the simulations, and necessary implementation of sub-grid SF and feedback recipes, means we are still not sure whether a violent major merger/interaction is absolutely necessary to produce a starburst or the strong Balmer absorption lines seen in post-starburst galaxies, or whether an AGN is necessary or able to halt the starburst rapidly enough to produce galaxy wide post-starburst features. Our catalogue of PSB regions in the galaxy-wide MaNGA survey allows us to address these questions from a new angle, compared to the single fibre surveys carried out in the past. With this new large and uniform IFU sample, we can get some new clues for understanding the origins of the PSB features.

For the CPSBs, the strong radial gradients in D_n4000 and $H\delta_A$ certainly support a scenario in which gas has flowed rapidly into the centre of the galaxy, leading to a strong central starburst. The high fraction ($\gtrsim$50 per cent) of objects with misaligned gas-star kinematics or tidal features supports the idea that a merger has triggered the gas inflow in the majority of cases. The globally young mass-weighted age indicates that a violent process has mixed the stars throughout the galaxy, and the significant decrease in stellar v/σ compared to the control sample again implies a violent interaction or merger has occurred. It seems unlikely that less violent processes, such as misaligned gas accretion from a neighbouring dwarf or the cosmic web could contribute significantly to the population. The weak W(Hα) throughout the disc implies subsequent galaxy-wide quenching of the SF, which could be caused by complete gas exhaustion, expulsion, or some additional heating mechanism. While AGN feedback has been postulated as a plausible mechanism for global quenching, it is unclear whether it can cause such galaxy-wide quenching in the relatively low-mass PSB galaxies present in our local Universe sample.

For the entirely new class of RPSBs, the strong radial gradient in W(Hα) compared to the control galaxies again suggests a recent strong inflow of gas to the central regions. 27 per cent of RPSBs show misaligned gas and star kinematics, 19 per cent have obvious bars, 30 per cent show interaction evidence like tidal tails, while the remainder are either face or edge-on making it difficult to identify bars or kinematic misalignment. All these mechanisms can lead to gas inflows (Lin et al. 2017; Chown et al. 2019), indicating that gas inflow is also key in the formation of the RPSBs. In contrast to the CPSBs, however, the RPSB galaxies have not (yet) suffered global quenching of the SF. The outer regions are identified as PSBs due to their weak W(Hα), however, typically the residual W(Hα) is still stronger than in the CPSBs. The presence of both RPSBs and IPSBs provides direct evidence that an AGN is not a necessary ingredient to rapidly quench a starburst and cause post-starburst features in galaxies.

The question that naturally arises is whether the RPSBs are simply younger relatives of the CPSBs, probing different evolutionary

phases of the same event. This would be consistent with the ongoing SF in the central regions of RPSBs, and higher fraction with clear evidence for tidal tails and interaction which fades rapidly with time since the starburst (Pawlik et al. 2018). If this were true it would also be tempting to suggest a scenario in which either the starburst or the quenching progresses from the outer regions inwards, the latter option presumably ruling out AGN feedback as the quenching mechanism. However, two lines of evidence suggest against this hypothesis. First, the two populations have very different SF histories at all radii (as indicated by their mass-weighted ages), and secondly the CPSBs have lower stellar v/σ at all radii. Neither of these observational features are alterable on time-scales of a few 100 Myr needed to shut down the central starburst in the RPSBs while retaining the strong Balmer absorption lines leading to the CPSB classification. We therefore conclude that the CPSB and RPSB galaxies are likely the product of different physical mechanisms.

In the Hα emission versus Hδ_A absorption plane, the RPSBs can be separated into two types: type I appear to be undergoing a global shutdown in SF which could plausibly be caused by strangulation processes where the infall of fresh gas is shut off; type 2 appears to require a more complex process with the outer regions quenching first while the inner regions remain star forming, perhaps caused by ram pressure stripping or interactions/mergers. Why these mechanisms would coincide with the requisite gas inflows to cause the central starburst remains unclear. In order to pin down the quenching mechanisms in different types of PSB galaxies, comparisons with detailed hydrodynamic simulations are clearly required.

5 SUMMARY

We identify galaxies with PSB regions in the MaNGA survey, generating a sample of 31 central (CPSBs), 37 ring (RPSBs), and 292 irregular (IPSBs) post-starburst galaxies. This is the first time that we are able to search for PSB regions across the full galaxy area, rather than focus on the central PSB regions. With this large IFU post-starburst sample, there are several important results that can be summarized as:

(i) Based on the global properties of the galaxies, we find that RPSBs are primarily located on the star-forming main sequence while CPSBs are primarily located in the green valley. While a higher fraction of CPSBs have Sérsic index $n > 3$ indicating pure spheroidal morphologies, CPSBs and RPSBs cover a wide range in n, showing that both types are hosted by galaxies with diverse morphologies.

(ii) Both CPSBs and RPSBs have positive gradients in D_n4000, indicating younger stellar populations in the central regions. This is different to control samples, which have flat or negative gradients.

(iii) While the CPSBs have suppressed SF throughout their bulge and disc, and clear evidence of rapid quenching in the central regions, the RPSBs only show clear evidence of recently rapidly suppressed SF in their outer regions and ongoing central SF/starburst.

(iv) The different radial profiles in mass-weighted age and stellar v/σ indicate that CPSBs and RPSBs are not simply different evolutionary stages of the same event, rather the CPSB galaxies are caused by a significant disruptive event, while the RPSB galaxies are more likely caused by disruption of gas fuelling to the outer regions.

(v) Compared to the control samples, both CPSB and RPSB galaxies show a higher fraction of interactions/mergers, misaligned gas, or bars that might be the cause of the gas inflows.

(vi) The presence of both RPSBs and IPSBs provide direct evidence that an AGN is not a necessary ingredient to cease starburst.

(vii) The wide range in observed radial profiles of Hα emission versus Hδ_A absorption in the RPSBs indicate that multiple processes may be responsible for their shut off in SF, such as strangulation processes where the infall of fresh gas is shut off leading to a global shutdown in SF, or ram pressure stripping or interactions/mergers leading to the rapid quenching of the outer regions while the inner regions remain star forming.

ACKNOWLEDGEMENTS

YC acknowledges support from the National Key R&D Program of China (No. 2017YFA0402700), the National Natural Science Foundation of China (NSFC grants 11573013, 11733002, 11922302). VW and KR acknowledge support of the European Research Council via the award of a starting grant (SEDMorph; P.I. V. Wild). CT acknowledges NSF CAREER Award AST-1554877. DB is partly supported by RSCF grant 19-12-00145. RR thanks CNPq, FAPERGS, and CAPES for partially funding this project. We thank MSc student John Proctor for carefully proof reading an early manuscript.

Funding for the Sloan Digital Sky Survey IV has been provided by the Alfred P. Sloan Foundation, the U.S. Department of Energy Office of Science, and the Participating Institutions. SDSS-IV acknowledges support and resources from the Center for High-Performance Computing at the University of Utah. The SDSS web site is www.sdss.org.

SDSS-IV is managed by the Astrophysical Research Consortium for the Participating Institutions of the SDSS Collaboration including the Brazilian Participation Group, the Carnegie Institution for Science, Carnegie Mellon University, the Chilean Participation Group, the French Participation Group, Harvard-Smithsonian Center for Astrophysics, Instituto de Astrofísica de Canarias, The Johns Hopkins University, Kavli Institute for the Physics and Mathematics of the Universe (IPMU) / University of Tokyo, Lawrence Berkeley National Laboratory, Leibniz Institut für Astrophysik Potsdam (AIP), Max-Planck-Institut für Astronomie (MPIA Heidelberg), Max-Planck-Institut für Astrophysik (MPA Garching), Max-Planck-Institut für Extraterrestrische Physik (MPE), National Astronomical Observatories of China, New Mexico State University, New York University, University of Notre Dame, Observatário Nacional / MCTI, The Ohio State University, Pennsylvania State University, Shanghai Astronomical Observatory, United Kingdom Participation Group, Universidad Nacional Autónoma de México, University of Arizona, University of Colorado Boulder, University of Oxford, University of Portsmouth, University of Utah, University of Virginia, University of Washington, University of Wisconsin, Vanderbilt University, and Yale University.

REFERENCES

Alatalo K., Cales S. L., Appleton P. N., Kewley L. J., Lacy M., Lisenfeld U., Nyland K., Rich J. A., 2014, ApJ, 794, L13
Alatalo K. et al., 2016a, ApJS, 224, 38
Alatalo K. et al., 2016b, ApJ, 827, 106
Baldry I. K., Glazebrook K., Brinkmann J., Ivezić Ž., Lupton R. H., Nichol R. C., Szalay A. S., 2004, ApJ, 600, 681

Baldwin J. A., Phillips M. M., Terlevich R., 1981, PASP, 93, 5
Balogh M. L., Miller C., Nichol R., Zabludoff A., Goto T., 2005, MNRAS, 360, 587
Bell E. F. et al., 2004, ApJ, 608, 752
Blanton M. R. et al., 2017, AJ, 154, 28
Brinchmann J., Charlot S., White S. D. M., Tremonti C., Kauffmann G., Heckman T., Brinkmann J., 2004, MNRAS, 351, 1151
Brough S. et al., 2017, ApJ, 844, 59
Brown M. J. I., Dey A., Jannuzi B. T., Brand K., Benson A. J., Brodwin M., Croton D. J., Eisenhardt P. R., 2007, ApJ, 654, 858
Bruzual A. G., 1983, ApJ, 273, 105
Bruzual G., Charlot S., 2003, MNRAS, 344, 1000
Bundy K. et al., 2015, ApJ, 798, 7
Cales S. L., Brotherton M. S., 2015, MNRAS, 449, 2374
Cappellari M., Copin Y., 2003, MNRAS, 342, 345
Cappellari M., Emsellem E., 2004, PASP, 116, 138
Cappellari M., 2016, ARA&A, 54, 597
Chabrier G., 2003, PASP, 115, 763
Chown R. et al., 2019, MNRAS, 484, 5192
Chen Y.-M. et al., 2016, Nat. Commun., 7, 13269
Davies R. L., Efstathiou G., Fall S. M., Illingworth G., Schechter P. L., 1983, ApJ, 266, 41
Dressler A., Gunn J. E., 1983, ApJ, 270, 7
Dressler A., Smail I., Poggianti B. M., Butcher H., Couch W. J., Ellis R. S., Oemler A. Jr, 1999, ApJS, 122, 51
Drory N. et al., 2015, AJ, 149, 77
Emsellem E. et al., 2007, MNRAS, 379, 401
Emsellem E. et al., 2011, MNRAS, 414, 888
Fischer J.-L., Domínguez Sánchez H., Bernardi M., 2019, MNRAS, 483, 2057
French K. D., Yang Y., Zabludoff A., Narayanan D., Shirley Y., Walter F., Smith J.-D., Tremonti C. A., 2015, ApJ, 801, 1
Goto T., 2005, MNRAS, 357, 937
Goto T., 2007a, MNRAS, 381, 187
Goto T., 2007b, MNRAS, 377, 1222
Goto T. et al., 2003a, PASJ, 55, 771
Goto T., Yamauchi C., Fujita Y., Okamura S., Sekiguchi M., Smail I., Bernardi M., Gomez P. L., 2003b, MNRAS, 346, 601
Green A. W. et al., 2018, MNRAS, 475, 716
Gunn J. E. et al., 2006, AJ, 131, 2332
Hawarden T. G., Mountain C. M., Leggett S. K., Puxley P. J., 1986, MNRAS, 221, 41P
Hiner K. D., Canalizo G., 2015, ApJ, 799, 59
Hogg D. W., Masjedi M., Berlind A. A., Blanton M. R., Quintero A. D., Brinkmann J., 2006, ApJ, 650, 763
Hopkins P. F., Hernquist L., Cox T. J., Di Matteo T., Robertson B., Springel V., 2006, ApJS, 163, 1
Hunter D. A., Elmegreen B. G., 2004, AJ, 128, 2170
Illingworth G., 1977, ApJ, 218, L43
Jin S.-W., Gu Q., Huang S., Shi Y., Feng L.-L., 2014, ApJ, 787, 63
Kauffmann G. et al., 2003, MNRAS, 346, 1055
Kaviraj S., Kirkby L. A., Silk J., Sarzi M., 2007, MNRAS, 382, 960
Kewley L. J., Dopita M. A., Sutherland R. S., Heisler C. A., Trevena J., 2001, ApJ, 556, 121
Kocevski D. D., Lemaux B. C., Lubin L. M., Shapley A. E., Gal R. R., Squires G. K., 2011, ApJ, 737, L38
Krajnović D., Cappellari M., de Zeeuw P. T., Copin Y., 2006, MNRAS, 366, 787
Lagos C. d. P., 2018, preprint (arXiv:1810.13074)
Law D. R. et al., 2015, AJ, 150, 19
Law D. R. et al., 2016, AJ, 152, 83
Lin L. et al., 2010, ApJ, 718, 1158
Lin L., Li C., He Y., Xiao T., Wang E., 2017, ApJ, 838, 105
Maltby D. T., Almaini O., Wild V., Hatch N. A., Hartley W. G., Simpson C., Rowlands K., Socolovsky M., 2018, MNRAS, 480, 381
Martin D. C. et al., 2007, ApJS, 173, 342
Naab T. et al., 2014, MNRAS, 444, 3357
Paccagnella A., Vulcani B., Poggianti B. M., Moretti A., Fritz J., Gullieuszik M., Fasano G., 2019, MNRAS, 482, 881
Pawlik M. M., Wild V., Walcher C. J., Johansson P. H., Villforth C., Rowlands K., Mendez-Abreu J., Hewlett T., 2016, MNRAS, 456, 3032
Pawlik M. M. et al., 2018, MNRAS, 477, 1708
Pawlik M. M., McAlpine S., Trayford J. W., Wild V., Bower R., Crain R. A., Schaller M., Schaye J., 2019, Nat. Asron., 3, 440
Poggianti B. M., Wu H., 2000, ApJ, 529, 157
Poggianti B. M., Smail I., Dressler A., Couch W. J., Barger A. J., Butcher H., Ellis R. S., Oemler A. Jr, 1999, ApJ, 518, 576
Pracy M. B., Couch W. J., Kuntschner H., 2010, Publ. Astron. Soc. Aust., 27, 360
Pracy M. B. et al., 2013, MNRAS, 432, 3131
Pracy M. B., Owers M. S., Zwaan M., Couch W., Kuntschner H., Croom S. M., Sadler E. M., 2014, MNRAS, 443, 388
Quintero A. D. et al., 2004, ApJ, 602, 190
Rowlands K., Wild V., Nesvadba N., Sibthorpe B., Mortier A., Lehnert M., da Cunha E., 2015, MNRAS, 448, 258
Rowlands K. et al., 2018, MNRAS, 473, 1168
Sánchez-Blázquez P. et al., 2006, MNRAS, 371, 703
Sánchez S. F. et al., 2016a, Rev. Mex. Astron. Astrofis., 52, 21
Sánchez S. F. et al., 2016b, Rev. Mex. Astron. Astrofis., 52, 171
Sell P. H. et al., 2014, MNRAS, 441, 3417
Smee S. A. et al., 2013, AJ, 146, 32
Socolovsky M., Almaini O., Hatch N. A., Wild V., Maltby D. T., Hartley W. G., Simpson C., 2018, MNRAS, 476, 1242
Swinbank A. M. et al., 2011, ApJ, 742, 11
Tran K.-V. H., Franx M., Illingworth G., Kelson D. D., van Dokkum P., 2003, ApJ, 599, 865
Tran K.-V. H., Franx M., Illingworth G. D., van Dokkum P., Kelson D. D., Magee D., 2004, ApJ, 609, 683
Tremonti C. A. et al., 2004, ApJ, 613, 898
Tremonti C. A., Moustakas J., Diamond-Stanic A. M., 2007, ApJ, 663, L77
van de Sande J. et al., 2017, MNRAS, 472, 1272
Veale M. et al., 2017, MNRAS, 464, 356
von der Linden A., Wild V., Kauffmann G., White S. D. M., Weinmann S., 2010, MNRAS, 404, 1231
Wake D. A. et al., 2017, AJ, 154, 86
Westfall K. B. et al., 2019, AJ, preprint (arXiv:1901.00856)
Wild V., Kauffmann G., Heckman T., Charlot S., Lemson G., Brinchmann J., Reichard T., Pasquali A., 2007, MNRAS, 381, 543
Wild V., Walcher C. J., Johansson P. H., Tresse L., Charlot S., Pollo A., Le Fèvre O., de Ravel L., 2009, MNRAS, 395, 144
Wild V., Heckman T., Charlot S., 2010, MNRAS, 405, 933
Wild V., Almaini O., Dunlop J., Simpson C., Rowlands K., Bowler R., Maltby D., McLure R., 2016, MNRAS, 463, 832
Wong O. I. et al., 2012, MNRAS, 420, 1684
Worthey G., Ottaviani D. L., 1997, ApJS, 111, 377
Worthey G., Faber S. M., Gonzalez J. J., Burstein D., 1994, ApJS, 94, 687
Yamauchi C., Yagi M., Goto T., 2008, MNRAS, 390, 383
Yan R., Newman J. A., Faber S. M., Konidaris N., Koo D., Davis M., 2006, ApJ, 648, 281
Yan R. et al., 2009, MNRAS, 398, 735
Yan R. et al., 2016a, AJ, 151, 8
Yan R. et al., 2016b, AJ, 152, 197
Yang Y., Zabludoff A. I., Zaritsky D., Lauer T. R., Mihos J. C., 2004, ApJ, 607, 258
Yang Y., Tremonti C. A., Zabludoff A. I., Zaritsky D., 2006, ApJ, 646, L33
Yang Y., Zabludoff A. I., Zaritsky D., Mihos J. C., 2008, ApJ, 688, 945
Yesuf H. M., Faber S. M., Trump J. R., Koo D. C., Fang J. J., Liu F. S., Wild V., Hayward C. C., 2014, ApJ, 792, 84
York D. G. et al., 2000, AJ, 120, 1579
Zabludoff A. I., Zaritsky D., Lin H., Tucker D., Hashimoto Y., Shectman S. A., Oemler A., Kirshner R. P., 1996, ApJ, 466, 104

This paper has been typeset from a TEX/LATEX file prepared by the author.